Mechanical Systems and Signal Processing 188 (2023) 109986

Contents lists available at ScienceDirect

Mechanical Systems and Signal Processing

journal homepage: www.elsevier.com/locate/ymssp

Nonlinear mechanical model of a fluid inerter

Miriam Chillemi [a], Thomas Furtmüller [a], Christoph Adam [a,*], Antonina Pirrotta [b]

[a] University of Innsbruck, Technikerstr. 13, 6020 Innsbruck, Austria
[b] University of Palermo, viale delle Scienze, 90128 Palermo, Italy

ARTICLE INFO

Keywords:
Structural control
Fluid inerter
Small-scale experiment
Modeling
Inertance

ABSTRACT

Dynamic vibration control devices provided with inertance, such as Tuned Inerter Dampers, Tuned Mass Damper Inerters or Tuned Liquid Column Damper Inerters, have been shown in numerous numerical studies to have superior vibration mitigation performance compared to conventional devices, such as Tuned Mass Dampers. One possible way to produce this inertance effect is by means of a moving fluid. In this study, the dynamic performance of such a fluid inerter is analyzed experimentally. The considered small-scale prototype consists of a hydraulic cylinder, and the inertance is generated by the flow of the working fluid in an external channel attached to the cylinder itself. In a first step, the dry configuration, i.e. without fluid, is investigated, revealing a nonlinear dissipation force. In a corresponding mechanical model, this force is represented by a variant of the well-known Stribeck effect. Subsequent experiments on the complete configuration, i.e. with fluid, reveal a further nonlinear effect. This effect is attributed to the compressibility of the working fluid as well as air trapped in the channel. Once the parameters of the mechanical model are retrieved, comparative studies are carried out. These show a remarkable agreement between numerical and experimental outcomes, thus enabling the mechanical model to be used in dynamic vibration control devices, as stated above.

1. Introduction

Natural disasters such as earthquakes and strong wind, or simply human activity, are sources of vibrations that might cause human discomfort or even damage to structural elements. At the same time, the evolution of computational mechanics and material sciences in civil engineering is leading to increasingly slender structures that are more prone to vibrations. The need to take into account architectural features while solving structural issues leads to so-called structural vibration control, i.e. the prevention and mitigation of vibrations [1]. Therefore, the development of innovative devices that can reduce and control large vibration amplitudes has been a flourishing research area in civil and mechanical engineering in recent years [2].

Control devices can be classified into four main categories according to their operation: passive, active, semi-active and hybrid [3]. Among them, passive vibration control systems are commonly used in construction due to their robustness. This type of device does not rely on an external power source and is usually cheaper and easier to maintain [4]. One example is Tuned Mass Dampers (TMDs), which have received considerable attention and recognition in the context of passive vibration control. TMDs reduce the displacement and/or acceleration demand of the vibration-prone structure by means of a viscously damped spring-mass system tuned to one natural frequency of the structure to which the device is attached [5]. Hence, tuned absorbers are widely used for structural control due to their simplicity and effectiveness. Nevertheless, it is important to note that the performance of the TMD strongly depends on its design [6]. One of the most important parameters to control is the mass itself. With increasing TMD mass,

* Corresponding author.
E-mail address: christoph.adam@uibk.ac.at (C. Adam).

https://doi.org/10.1016/j.ymssp.2022.109986
Received 23 August 2022; Received in revised form 17 November 2022; Accepted 22 November 2022
Available online 5 December 2022
0888-3270/© 2022 The Author(s). Published by Elsevier Ltd. This is an open access article under the CC BY license (http://creativecommons.org/licenses/by/4.0/).

the efficiency also increases, but on the other hand, there is an undesirable additional weight for the structure. For this reason, the TMD mass is generally taken to be no larger than 5% of the mass of the main structure.

With this in mind, an auxiliary device that can increase this mass without interfering with the design process of the structure would result in a more desirable scenario. The so-called inerter is particularly suitable for this purpose. Inerters were first introduced in 2002 by Smith [7] and have since then been widely used in suspension systems for Formula 1 cars. Nowadays, however, they are also employed in other fields, such as suspension of railway vehicle, passive walking of bipedal robots, steering oscillations of motorcycles, and, in general, vibration control devices [8]. The inerter fictitiously increases the mass of the structure to which it is connected, allowing a mass amplification effect without adding any physical mass to the system. The generated apparent mass may be very large and can be used in combination with springs and dashpot dampers (referred to as Tuned Inerter Dampers, TIDs) [9] or exploited to improve the performance of various mass-dependent control devices. In this regard, Tuned Mass Damper Inerters (TMDIs) outclasses the traditional TMD performance controlling structural vibration with an increased mass, which at the same time does not address physical load to the main structure [10]. Another interesting alternative relies in the so-called Tuned Liquid Column Damper Inerter (TLCDI), where a tank hosting fluid (usually water) is capable of translational motion on sliding support while being connected to the structure through a spring and a dashpot and to the ground through the inerter. In this case the vibrations mitigation is due to the combination of both the effect of the vertical motion of the liquid inside the container and its horizontal translational motion [11]. Furthermore, other energy dissipation devices have been discussed in literature [12,13]. In these cases, the apparent mass-amplification effect is achieved by an inerter placed in parallel with a viscous damper. Inertial mass dampers have also been studied in combination with base isolation systems to prevent seismic risk [14,15].

So far, among all the different built and prototyped inerters, the most common types are rack and pinion inerters [16], ball-screw inerters [17], and fluid inerters [18]. The first two types are mechanical inerters that need a flywheel to achieve the inertia effect. Instead, fluid inerters usually consist of hydraulic systems without a flywheel [19]. Here, the inerter effect is achieved by a flow of fluids through some external channels [20]. While mechanical inerters have been widely analyzed experimentally [21–24], application and experimental verification of fluid inerters are scarce. However, the latter offer some advantages over mechanical devices. Fluid inerters are easier to design and develop and can be adapted to implement several damper arrangements [25], especially for larger civil structures. Further, parasitic effects such as backlash and ratcheting are less pronounced than with mechanical devices [26]. Thus, fluid-based inerters can mitigate the aforementioned drawbacks with a fairly simple design and very low maintenance requirements.

For these reasons, the present study aims at characterizing the dynamic properties of a fluid inerter. In particular, an accurate mechanical model of the device and its parameters is determined, which provides more realistic numerical predictions than a common linear model. It should be mentioned that previous studies with similar objective can be found in the literature. In [27], the nonlinear mechanical model of a fluid inerter is derived based on a hydraulic model. The model is verified by an experimental campaign, but presented only for certain frequencies. Unlike [27], the mechanical properties of the fluid inerter model are directly addressed in the present study. As will be demonstrated in Section 4, this leads to a more accurate definition of the dissipation force and nonlinearity due to the compressibility of fluid and air. Furthermore, sine sweep tests are performed in the present study to compare the experimental and numerical outcomes continuously in a frequency range from 1 to 10 Hz.

This paper is organized as follows: In Section 2, the working principle of fluid inerters and the origin of the inertance is outlined briefly. In Section 3, the experimental setup is described and results of the tests are presented. Appropriate mechanical models for the two considered states (without and with water) are developed in Section 4, while the parameters of these models are identified in Section 5 based on the experimental data.

2. Working principle of fluid inerters

In a lumped model, an inerter can be treated as a two-terminal device analogously to springs and dampers in which the internal force F_I is proportional to the relative acceleration between the two terminals [7],

$$F_I(t) = b(\ddot{x}_2(t) - \ddot{x}_1(t)) \tag{1}$$

The constant of proportionality is called inertance and denoted by the letter b, and $\ddot{x}_1$ and $\ddot{x}_2$ are the total accelerations of the terminals 1 and 2, respectively. The most common configuration of a fluid inerter is illustrated in Fig. 1. Such a layout includes a piston with a through rod that slides in a cylinder filled with a hydraulic fluid (usually water or oil) and equipped with a helical tube connecting the two terminals of the piston. The flow of the fluid through the cylinder and the helical pipe is due to the movement of the piston relative to the cylinder itself. The inertance b has the dimension of a mass (kilogram) and depends on the way the inerter is designed. It can be derived as follows [28],

$$b = \frac{m_{fluid}}{1 + \left(\frac{h}{2\pi r_h}\right)^2} \left(\frac{A_1}{A_2}\right)^2 \tag{2}$$

where A_1 and A_2 denote the cross-sectional area of the main cylinder minus the rod and the helical tube, respectively, h represents the pitch of the helical channel, and r_h is its helix radius. Due to the inertia effect, the mass of the fluid m_{fluid} is expected to be significantly smaller than the inertance b. In particular, it has been observed that the magnification scale can be as large as 10,000 [29].

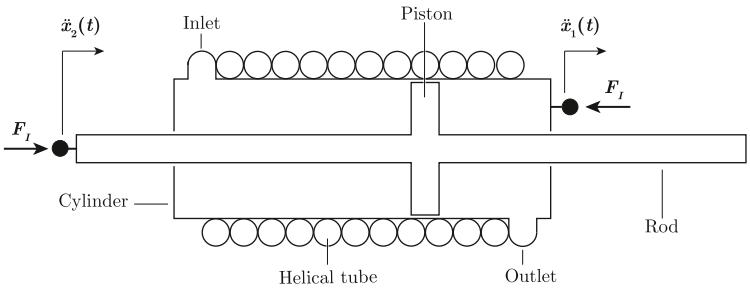

Fig. 1. A two-terminal mechanical network in a free-body diagram of a fluid inerter [18].

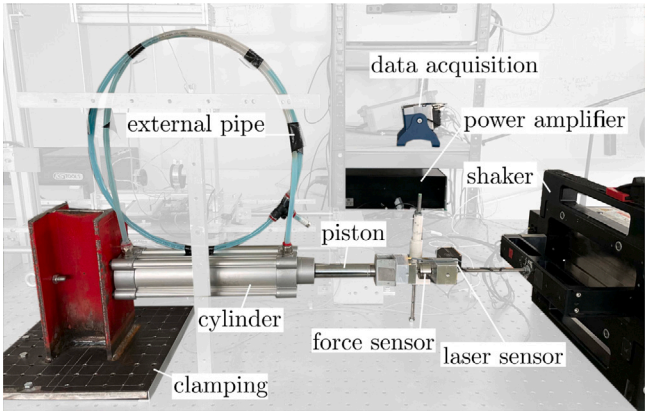

Fig. 2. Test setup of the small-scale prototype of the fluid inerter.

3. Experimental setup

3.1. Prototype design

Fig. 2 shows the experimental setup for the small-scale prototype of a fluid inerter developed at the Unit of Applied Mechanics, University of Innsbruck. The prototype consists of a cylinder barrel in which a piston, connected to a piston rod, moves back and forth. The barrel is closed at one end by the cylinder bottom and rigidly connected to an IPE steel profile that serves as a clamping. The other terminal is the cylinder head, which is connected to an electro-dynamic shaker that provides the input force. The piston divides the inside of the cylinder into two chambers and is equipped with sliding rings and rubber seals to prevent flow between the chambers. Water was chosen as the working medium due to its properties and ease of use and availability. The inertia effect therefore results from the flow in the external channel, which is attached to the cylinder by means of two watertight valves. For practical reasons, the pipe is not wrapped around the main cylinder, as it is usually shown in the literature (Fig. 1), but is arranged as a ring directly above the hydraulic actuator. It has been observed that this arrangement does not impair the beneficial characteristics of the inerter. The properties of the prototype described above are listed in Table 1 and graphically summarized in Fig. 3. Employing Eq. (2), the inertance is predicted to be $b = 163$ kg, while the actual mass of the device including cylinder, piston, and external pipe is approximately 2 kg and the mass of the working fluid is only about 50 g.

3.2. Considered configurations

Due to the physical nature of hydraulic systems, such as hydraulic cylinders, careful consideration must be given to the nonlinearity introduced by friction [30]. With the aim of deriving an appropriate friction model for the system, the device was first examined in dry conditions, i.e., without the presence of the working fluid, compare with Fig. 4. Once the tribological characteristics of the device without water were known, the inertial properties of the complete system were studied, included the fluid, as schematically depicted in Fig. 5.

3.3. Excitation and data acquisition

Both configurations of the system were dynamically excited by an APS 400 Electro-Seis long-stroke shaker from APS Dynamics, Inc. and driven by an APS 145 power amplifier. In both configurations, the displacement of the piston was recorded by an optical

Table 1
Parameters of the small-scale prototype.

Parameter	Symbol	Value
Stroke length [mm]	L_c	200
Cylinder ∅ [mm]	D_c	50
Piston rod ∅ [mm]	D_p	20
Piston mass [kg]	m_p	1
Cross-sectional area of the cylinder minus the rod [m^2]	A_1	1.64×10^{-3}
External pipe ∅ [mm]	D_h	6
External pipe length [m]	l_h	1.7
Cross-sectional area of external pipe [m^2]	A_2	0.028×10^{-3}
Working fluid density [kg m^{-3}]	ρ	995.6
Working fluid mass [kg]	m_l	0.048
Inertance [kg]	b	163
Cylinder barrel material	–	Anodized aluminum
Cylinder heads material	–	Die-cast aluminum
Piston material	–	Chromed steel
Seals material	–	Nitrile rubber

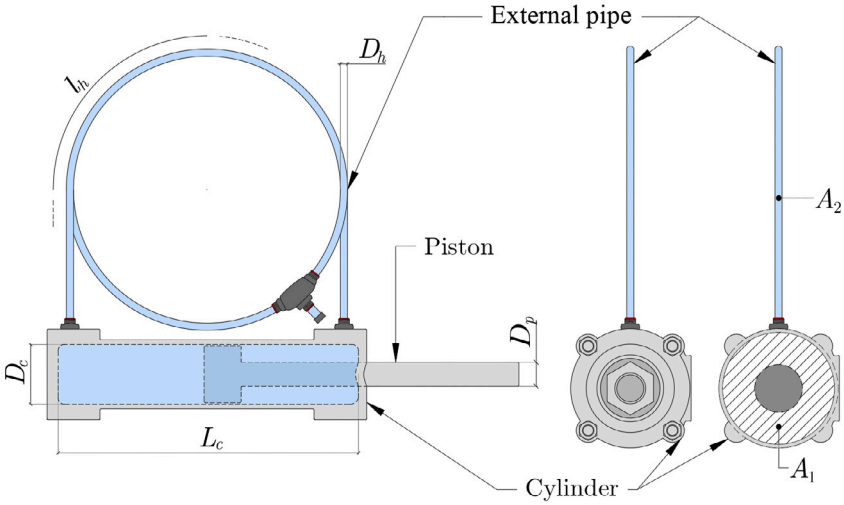

Fig. 3. Sketch of the side and front view of the small-scale prototype of the hydraulic inerter.

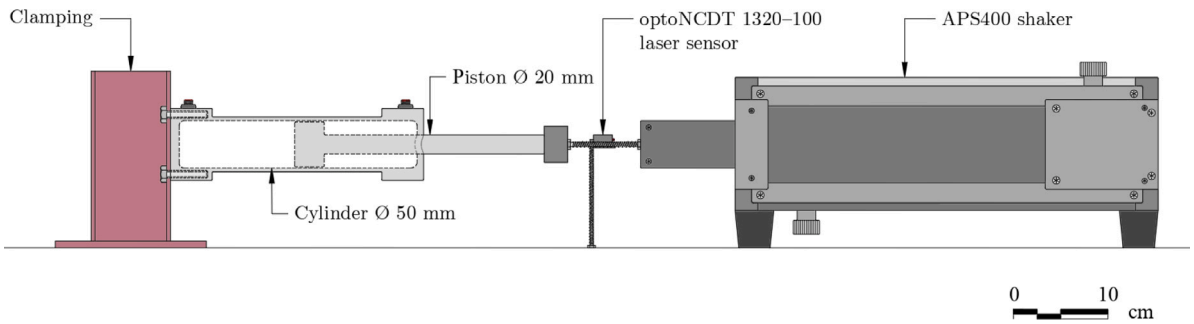

Fig. 4. Dry configuration scheme.

laser sensor of type optoNCDT 1320–100 from Micro-Epsilon Messtechnik GmbH, and the force was measured by a load cell of type KM26z from ME-Meßsysteme. A National Instruments CompactDAQ (NI cDAQ) system controlled by a MATLAB script was used for signal generation and data acquisition. A linear sweep (chirp) in the frequency range from 0.5 to 12 Hz in a time period of 60 s with increasing input voltage amplitude served as excitation signal to the power amplifier. As an example, Fig. 6 shows the input voltage signal linearly increasing from 0.35 V to 0.55 V. By changing the magnitude of the voltage input, different excitation amplitudes were considered to reveal nonlinear effects.

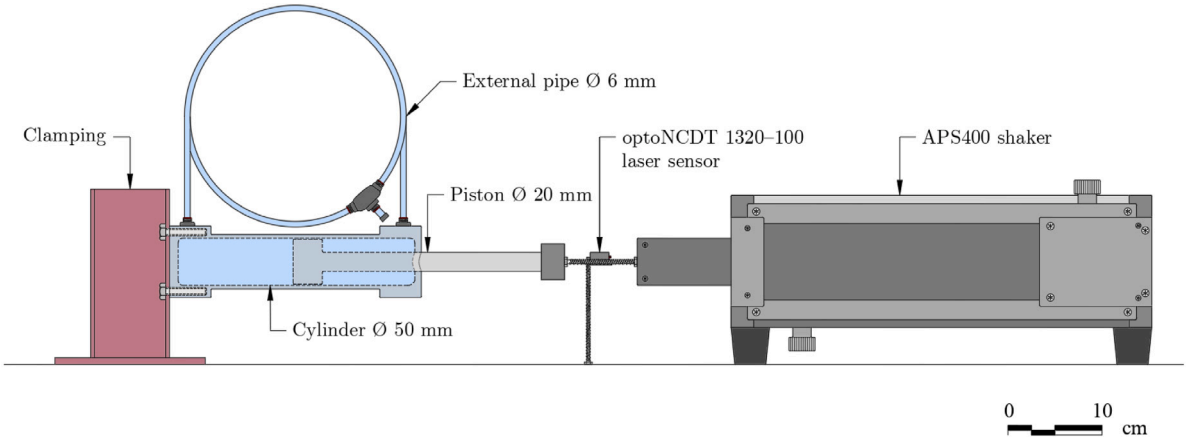

Fig. 5. Complete configuration scheme.

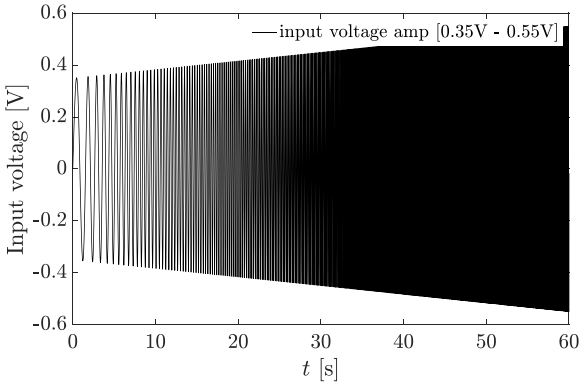

Fig. 6. Sine sweep input signal with increasing voltage amplitude.

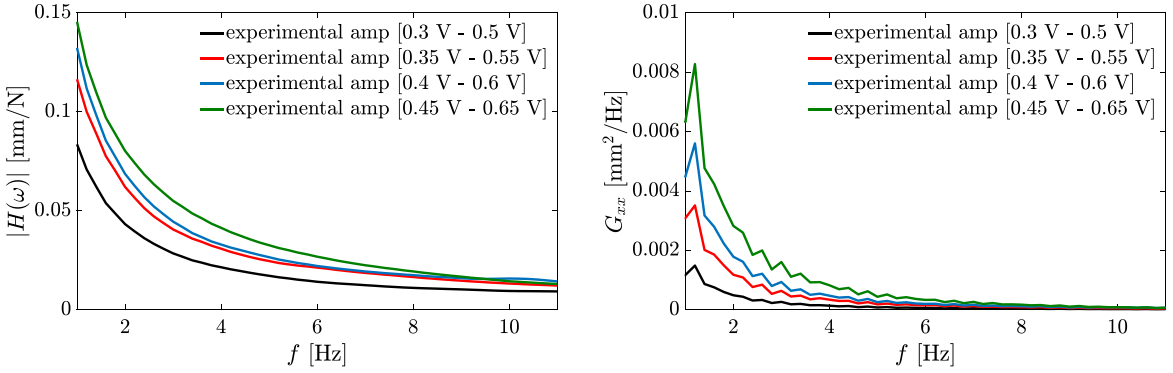

Fig. 7. Experimental results in terms of receptance (left) and PSD (right) for different excitation signal amplitudes in the dry configuration.

3.4. Experimental outcomes

As a result of the experiments, Fig. 7 shows for the dry configuration the receptance magnitude $|H(\omega)|$ (i.e., the ratio of displacement over input force) and the power spectral density (PSD) G_{xx} of the displacement for different ranges of the input voltage signal. As can be seen, with increasing amplitude of the input voltage signals, the amplitudes of both $|H(\omega)|$ and G_{xx} increase, indicating a nonlinear effect due friction between the piston rod and cylinder.

This nonlinearity is less pronounced in the complete configuration, as will be shown in Section 5. However, a strong influence of a static preload of the system was observed. To this end, the sine sweep excitation was preceded by a constant input voltage

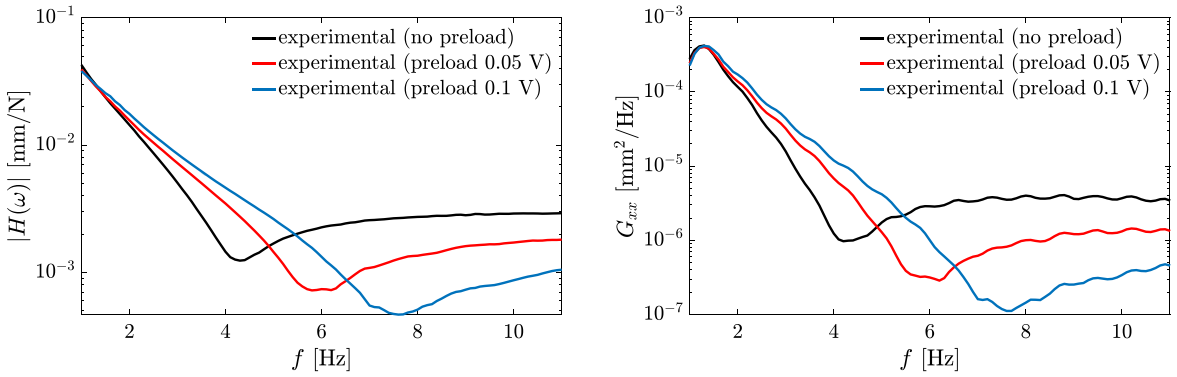

Fig. 8. Experimental results in terms of receptance (left) and PSD (right) for different preload magnitudes in the complete configuration.

signal to prestress the system. In Fig. 8 experimental outcomes are shown for two different preload amplitudes as well as for the case without prestress. An anti-resonance is observed which shifts to higher frequencies with increasing preload magnitude. This suggests that the piston mass and the fictitious mass due to the flowing fluid do not oscillate as one mass, but that there is a relative displacement between the two masses. Hence, two mechanical degrees of freedom are used in the next section to model this effect.

4. Mechanical models

In order to numerically reproduce the experimental results and to perform a parametric study in further research, mechanical models of the two configurations considered were developed. Based on preliminary tests, it was found that the friction force depends on both the position of the piston and the direction of movement. However, this also affects the recorded input force, leading to an asymmetrical curve due to the aforementioned irregularities of the friction force. With the aim of considering the simplest possible (deterministic) inerter model, the simulations were not performed on a purely mechanical model subjected to force input. Instead, the vibration exciter was included in the simulation model, resulting in an electro-mechanical system whose input signal is the same voltage signal as in the experimental studies.

4.1. Vibration exciter

Following the study presented in [31], the electro-dynamic shaker is modeled as a two degree-of-freedom (DOF) system, with shaker displacement $x_1(t)$ and electrical current $i(t)$ as DOFs. The force provided by the exciter is proportional to the magnetic flux passing through a coil, to the current flowing through the coil, and to the length of wire within the flux field [31]. Generally, it can be assumed that the mechanical part of the vibration exciter consists of the coil and the table structure, jointly referred to as armature assembly and modeled as a lumped armature mass m_s. This mass is connected to the ground via a Kelvin-Voigt element with spring stiffness k and damping coefficient c. On the other hand, the electrical model of the shaker must account for the presence of resistance R and inductance L featured in the coil. The interaction between the electrical and mechanical domains consists in the movement of the coil in the magnetic field, which generates a voltage on the coil itself. Therefore, the mechanical system is excited by a force F proportional to the current through the constant α_1, while the electrical circuit is excited by an internal voltage proportional to the velocity through the constant α_2. Dropping the elements m_p and f_{diss} in Fig. 9, this figure shows then the electromechanical model of the vibration exciter, where $u(t)$ is the input voltage. The equations of motion of the vibration exciter with 2-DOF system read as [31]

$$\mathbf{M}\,\ddot{\mathbf{x}} + \mathbf{C}\,\dot{\mathbf{x}} + \mathbf{K}\mathbf{x} = \mathbf{f} \tag{3}$$

where a dot over a variable stands for derivation with respect to time. The matrices $\mathbf{M}$, $\mathbf{C}$, $\mathbf{K}$ and the vectors $\mathbf{x}$ and $\mathbf{f}$ are

$$\mathbf{M} = \begin{bmatrix} m_s & 0 \\ 0 & 0 \end{bmatrix}, \quad \mathbf{C} = \begin{bmatrix} c & 0 \\ \alpha_2 & L \end{bmatrix}, \quad \mathbf{K} = \begin{bmatrix} k & -\alpha_1 \\ 0 & R \end{bmatrix},$$
$$\mathbf{x} = \begin{Bmatrix} x_1(t) \\ i(t) \end{Bmatrix}, \quad \mathbf{f} = \begin{Bmatrix} 0 \\ u(t) \end{Bmatrix} \tag{4}$$

Based on values provided in the shaker and power amplifier datasheets [32], and by trial-and-error, the parameters in the equations of motions were obtained as given in Table 2.

Fig. 10 compares the magnitude of the shaker transfer function, i.e., the ratio of the acceleration of the armature mass $\ddot{x}_1$ to the input voltage u, from an experiment and from an analysis with the system of Eqs. (3). As observed, both curves are in excellent agreement. In the underlying experiment, the acceleration of the shaker armature was recorded with a piezoelectric accelerometer of type 4508 from Bruel&Kjaer.

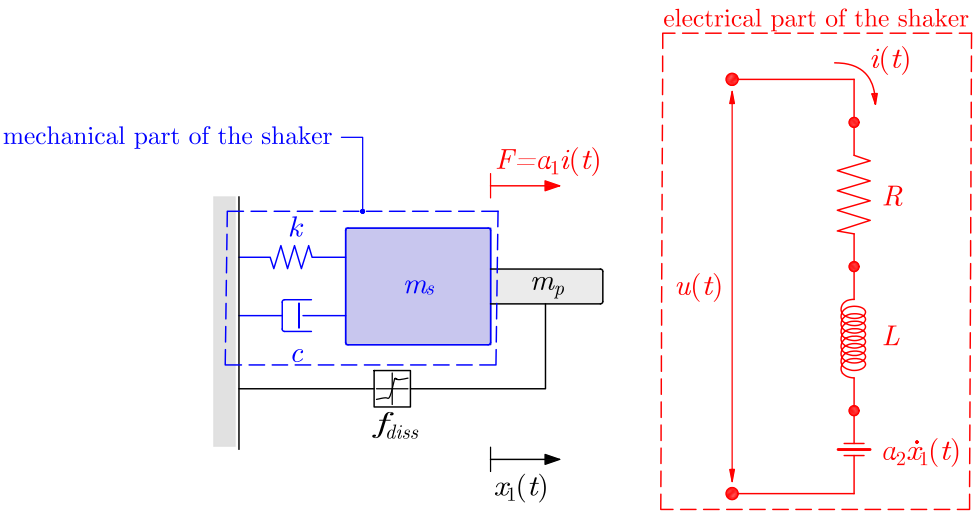

Fig. 9. Electro-mechanical model of the shaker alone (mechanical part plotted in blue, electrical part plotted in red) and of the dry configuration plotted in grayscale.

Table 2
Properties of the vibration exciter.

Parameter	Symbol	Value
DC Coil Resistance [Ω]	R	1.75
Inductance [H]	L	0.022
Force-current ratio [N/A]	α_1	20
Voltage-velocity ratio [V/(m/s)]	α_2	20
Gain voltage mode [V/V]	G	19
Armature assembly mass [kg]	m_a	2.7
Stiffness [N/m]	k	106.59
Damping coefficient [Ns/m]	c	6.79

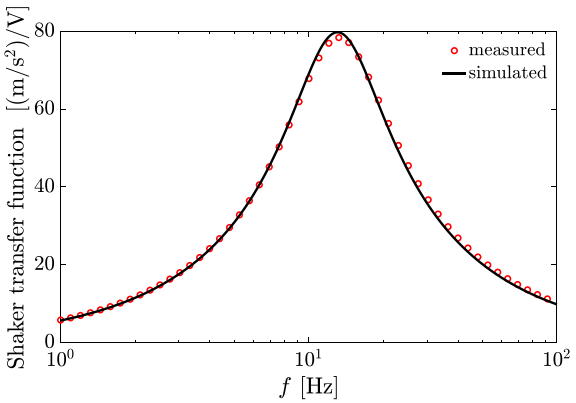

Fig. 10. Shaker transfer function between input voltage and output acceleration, based on the numerical model and an experiment.

4.2. Dry configuration

In the dry configuration shown schematically in Fig. 4, the piston rod of the hydraulic cylinder is rigidly attached to the terminal of the shaker. Hence, in the mechanical model in Fig. 9, the piston mass m_p is rigidly connected to the armature mass m_s. To model the friction between piston rod and cylinder, a dissipation force element f_{diss} is introduced, which is assumed to be a function of

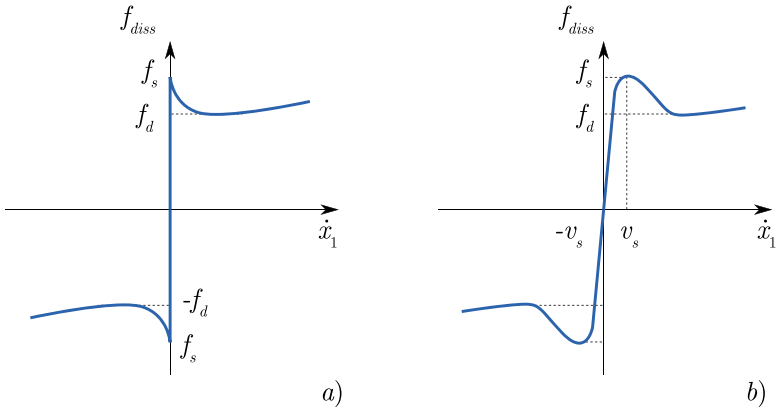

Fig. 11. (a) Classical representation of the Stribeck effect [36]. (b) Alternative friction model proposed in [37].

the velocity $\dot{x}_1$ [33]. Hence, no additional DOF is introduced, but the matrices **M**, **C**, **K** and the vectors **x** and **f** in Eqs. (3) now read

$$\mathbf{M} = \begin{bmatrix} m_s+m_p & 0 \\ 0 & 0 \end{bmatrix}, \quad \mathbf{C} = \begin{bmatrix} c & 0 \\ \alpha_2 & L \end{bmatrix}, \quad \mathbf{K} = \begin{bmatrix} k & -\alpha_1 \\ 0 & R \end{bmatrix},$$
$$\mathbf{x} = \begin{Bmatrix} x_1(t) \\ i(t) \end{Bmatrix}, \quad \mathbf{f} = \begin{Bmatrix} -f_{diss}(\dot{x}_1(t)) \\ u(t) \end{Bmatrix} \tag{5}$$

Standard ODE solvers cannot be used to compute the response of this nonlinear system of equations, because the matrix **M** contains zero elements on the main diagonal and thus the inverse $\mathbf{M}^{-1}$ cannot be computed. To avoid poor computational efficiency by using implicit ODE solvers, the electric charge q is employed as electrical quantity instead of the current i. By applying the relations [34]:

$$\dot{q}(t) = i(t), \quad \ddot{q}(t) = \frac{di}{dt} \tag{6}$$

the matrices and vectors of Eq. (5) can be recast as

$$\mathbf{M} = \begin{bmatrix} m_s+m_p & 0 \\ 0 & L \end{bmatrix}, \quad \mathbf{C} = \begin{bmatrix} c & -\alpha_1 \\ \alpha_2 & R \end{bmatrix}, \quad \mathbf{K} = \begin{bmatrix} k & 0 \\ 0 & 0 \end{bmatrix},$$
$$\mathbf{x} = \begin{Bmatrix} x_1(t) \\ q(t) \end{Bmatrix}, \quad \mathbf{f} = \begin{Bmatrix} -f_{diss}(\dot{x}_1(t)) \\ u(t) \end{Bmatrix} \tag{7}$$

Now the inverse $\mathbf{M}^{-1}$ can be computed in such a way that the system of Eqs. (3) can be reformulated as first-order system, which can be solved, for instance, in MATLAB by the standard *ode45* solver.

Contrary to the suggestions in [35], it was found that due to a pronounced stick–slip phenomenon that occurred during experimental tests, a rather simple friction model, such as the Coulomb one, is not suitable to model the system behavior. In particular, it was observed that friction at or near zero velocity $v = \dot{x}_1$ is greater than friction at higher velocities. This phenomenon is the so-called Stribeck effect, whose classical representation is illustrated in Fig. 11 (a) [36]. As can be seen, two different forces are involved, commonly referred to as static friction (or stiction) f_s and dynamic friction (or Coulombic friction) f_d. Additionally, friction also exhibits viscous characteristics at contacts between lubricated surfaces, such as the piston rod sliding back and forth through the cylinder head, resulting in a viscous force that increases linearly with v. However, in analytical simulations, this model may suffer from numerical instability due to the discontinuity of the friction force at zero velocity.

To overcome this numerical inconveniences, several alternatives have been proposed in the literature. In [30], it was found that the Brown–McPhee approach [37] is numerically the most efficient model for describing the friction properties in the dynamic simulation of hydraulic actuators. This model shown in Fig. 11 (b) is able to capture the effects of static, dynamic, and viscous friction just discussed, employing a continuous and differentiable equation. In the graph of Fig. 11 (b), v_s is the so-called Stribeck velocity and corresponds to the velocity value occurring when the maximum static friction is experienced. Starting from this point, the force decreases with increasing velocities until reaching f_d. Subsequently, the viscous friction term begins to be predominant and the dissipation force increases again with a linear trend. Based on [37], for the dissipation force the function

$$f_{diss}(\dot{x}_1) = \left(f_d \tanh\left(4\frac{|\dot{x}_1|}{v_s}\right) + (f_s - f_d)\frac{\frac{|\dot{x}_1|}{v_s}}{\left(\frac{1}{4}\left(\frac{|\dot{x}_1|}{v_s}\right)^2 + \frac{3}{4}\right)^2} \right) \mathrm{sgn}(\dot{x}_1) + c_s\,\dot{x}_1 \tag{8}$$

is introduced in Eqs. (7) with the four friction properties f_s, f_d, v_s and c_s to be identified.

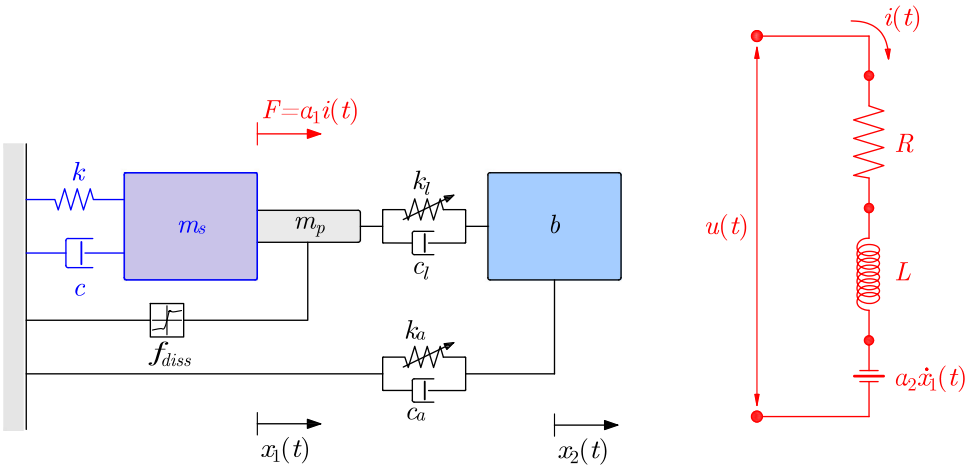

Fig. 12. Electro-mechanical model of the complete configuration.

4.3. Complete configuration

Once equipped with the external pipe and filled with water, the electro-mechanical model of the complete configuration as shown in Fig. 12 is considered. Compared to the arrangement of the dry configuration, an additional DOF is introduced to model the effect of the inertial mass b due to the water flow in the external pipe. Based on the observations of the experimental campaign, it is linked to the piston rod mass through a nonlinear spring-viscous damper (NSD) element, which models the fluid behavior, and to the ground through another NSD element, which in this case models the behavior of the air inside the system. In total, the model of the complete configuration consists of an electrical DOF $q(t)$ and two mechanical DOFs $x_1(t)$ and $x_2(t)$, corresponding to the relative displacement of the piston and the water mass with respect to the ground. Eqs. (3) govern the response of the complete configuration when the matrices **M**, **C**, **K** and the vectors **x** and **f** are modified as follows,

$$\mathbf{M}=\begin{bmatrix} m_s+m_p & 0 & 0 \\ 0 & b & 0 \\ 0 & 0 & L \end{bmatrix}, \quad \mathbf{C}=\begin{bmatrix} c+c_l & -c_l & -\alpha_1 \\ -c_l & c_l+c_a & 0 \\ \alpha_2 & 0 & R \end{bmatrix}, \quad \mathbf{K}=\begin{bmatrix} k & 0 & 0 \\ 0 & 0 & 0 \\ 0 & 0 & 0 \end{bmatrix},$$
$$\mathbf{x}=\begin{Bmatrix} x_1(t) \\ x_2(t) \\ q(t) \end{Bmatrix}, \quad \mathbf{f}=\begin{Bmatrix} -f_{diss}(\dot{x}_1)-k_l(x_1,x_2)(x_1-x_2) \\ -k_l(x_1,x_2)(x_2-x_1)-k_a(x_2)x_2 \\ u(t) \end{Bmatrix} \tag{9}$$

While the fluid is an integral part of the system, the air trapped in the external is an undesired, but in the experience of the authors, unavoidable effect. Moreover, it was found that the volume of the air in the pipe increases with increasing preload and excitation intensity. This effect can be explained with the cavitation phenomena [20], i.e., the formation and growth of bubbles when the absolute pressure in the fluid is close to that of saturated vapor for the temperature of water. With this in mind, the parameters for modeling the air NSD element need to be updated according to the different conditions of the system. To characterize the nonlinear air spring stiffness, the following relationship is used [38],

$$k_a(x_2)=\gamma\ A_2^2\frac{p_0}{V_0}\cdot\left[1-\frac{A_2}{V_0}x_2\right]^{-(\gamma+1)} \tag{10}$$

which was originally introduced to model this effect in Tuned Liquid Column Dampers. In Eq. (10), p_0 is the atmospheric pressure, V_0 is the volume of the air column, and $\gamma = 1.4$ is the specific heat ratio. In order to model the increasing air volume, the length of the air column was measured in each step, as shown in Fig. 13. Consequently, V_0 in Eq. (10) is changed according to the different geometry of the air column endured during the tests. The same applies to the air dashpot with parameter c_a. That is, c_a is small and practically irrelevant when the device has not experienced any preload, but becomes larger and thus significant with increasing preload.

For the fluid NSD element, an expression similar to Eq. (10) is adopted. With $\gamma = 1$, the general form

$$k_l(x_1,x_2)=k_0\cdot\left[1-k'\left(x_2-x_1\right)\right]^{-2} \tag{11}$$

is obtained where the initial stiffness k_0 and the slope k' are the material properties to be identified. It should be emphasized that this model copes with the problem encountered in previous studies [27] in which the fluid spring value is updated for each testing amplitude without an underlying mechanical model.

Unlike the air dashpot parameter c_a, the fluid dashpot parameter c_l does not need to be updated as the preload values increase because it does not undergo severe changes in its physical or geometrical properties that require modifications in the model. Hence,

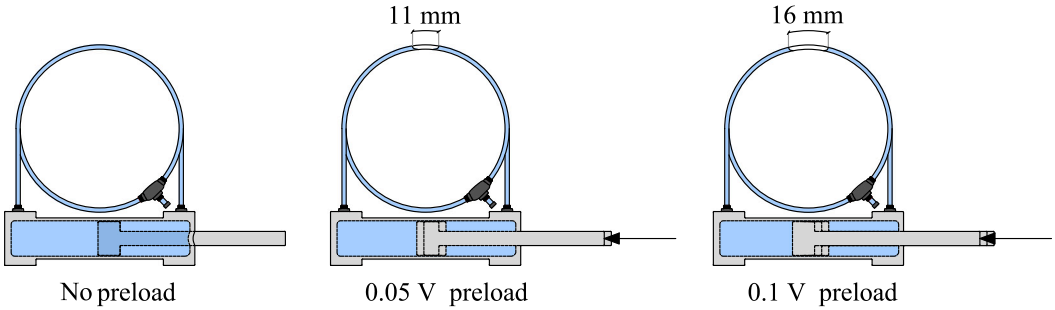

Fig. 13. Increasing air column length with increasing preload values.

Table 3
Identified properties of the dissipation force model.

Parameter	Symbol	Value
Static friction force [N]	f_s	50
Dynamic friction force [N]	f_d	25
Stribeck velocity [m/s]	v_s	0.013
Viscous friction parameter [Ns/m]	c_s	515

Table 4
Identified properties of NSD elements in the complete configurations.

Parameter	Symbol	Value
Initial fluid spring stiffness [N/m]	k_0	1.25×10^5
Fluid spring slope [1/m]	k'	43
Fluid damping coefficient [Ns/m]	c_l	950
Air damping coefficient, 0.05 V preload [Ns/m]	c_a	300
Air damping coefficient, 0.1 V preload [Ns/m]	c_a	700

a constant value of c_l is employed for each preload step. Specifically, the total fluid damping force is meant to model the viscous shear friction that arises in the external channel due to the fluid flow as well as its pressure drop and the port losses [20].

5. Numerical simulations

In this section, the yet unknown parameters of the two considered configurations are derived by numerical simulations and optimization with respect to the experimental outcomes presented in Section 3.4. The *GlobalSearch* function implemented in MATLAB was used, employing the *fmincon* optimization algorithm. Both the sum of the squared errors of the receptances and the PSDs serve as objective function. Note that it is not sufficient to consider solely the receptance in the comparisons for this nonlinear system, as other objective function minima may then be found where both the displacement and force are incorrect, but the errors cancel out when the receptance is computed.

5.1. Dry configuration

Table 3 lists the parameters for the model of the dissipation force according to Eq. (8) obtained by numerical optimization, while Figs. 14 and 15 compare the receptance magnitudes and PSDs, respectively, for all four input voltage amplitude ranges considered. Solid black lines refer the experimental results and solid blue lines with markers indicate the numerical ones. The comparison demonstrates that results of experiment and simulation match almost perfectly, especially for larger amplitude ranges.

In addition to these comparisons in frequency domain, in Fig. 16 segments of 10 s duration are shown in time domain. From this figure it is seen also the phase of the experimental and numerical outcomes show excellent correlation for all amplitudes considered.

5.2. Complete configuration

For the complete configuration, it is assumed that the friction model does not change, i.e., f_{diss}, according to the parameters given in Table 3, hold. The remaining parameters of the fluid and air NSD elements obtained by numerical optimization are given in Table 4.

Figs. 17 and 18 compare the receptance magnitudes and PSDs for the three considered preload levels, where the solid black lines represent the experimental results and solid blue lines with markers the analytical ones. The agreement is very close, particularly with respect to the location of the anti-resonance frequency. Minor deviations in the frequency range below 3 Hz in the case of zero

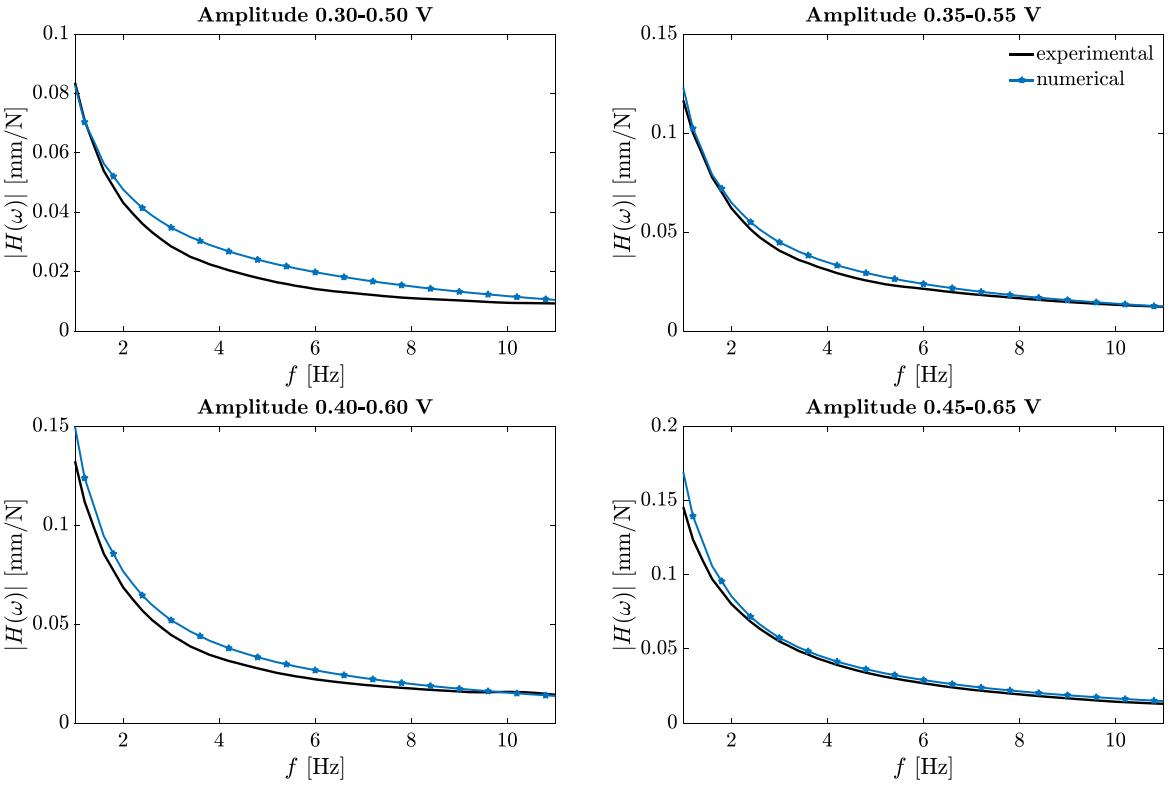

Fig. 14. Experimental (solid black line) versus numerical (solid blue line with markers) receptance response.

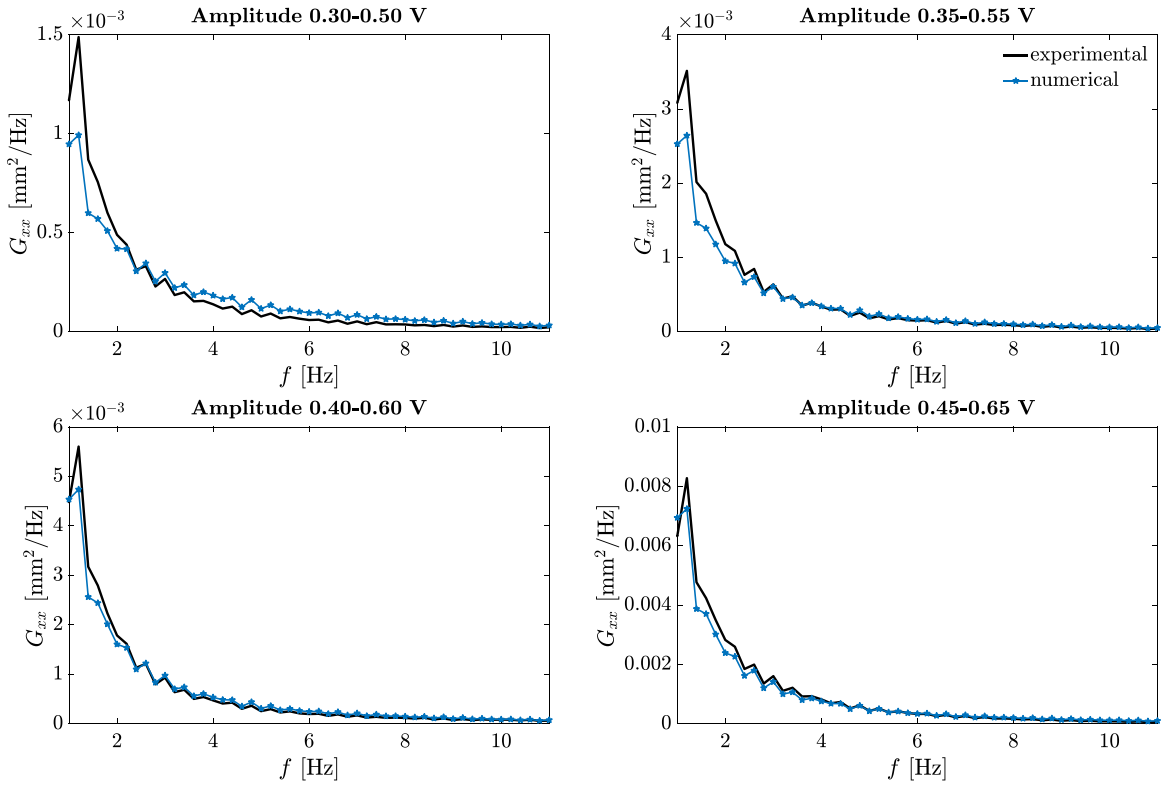

Fig. 15. Experimental (solid black line) versus numerical (solid blue line with markers) PSD response.

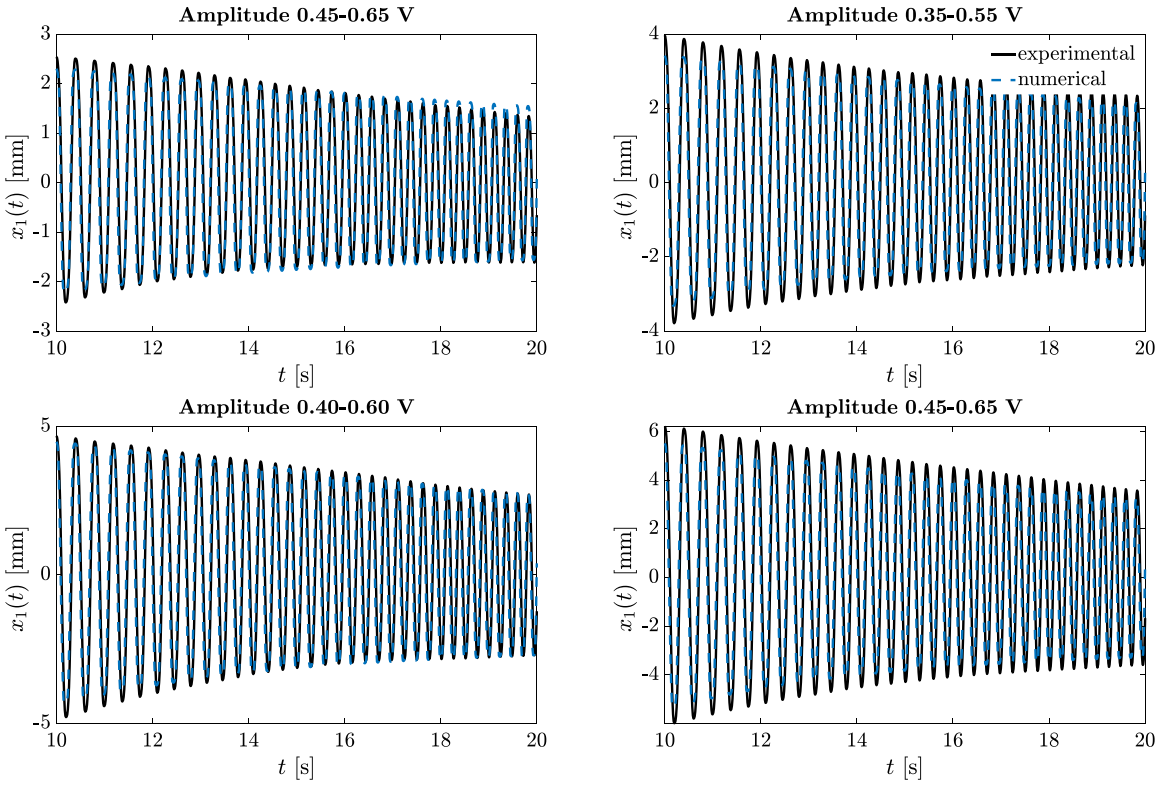

Fig. 16. Experimental (solid black line) versus numerical (dashed blue line) displacement response.

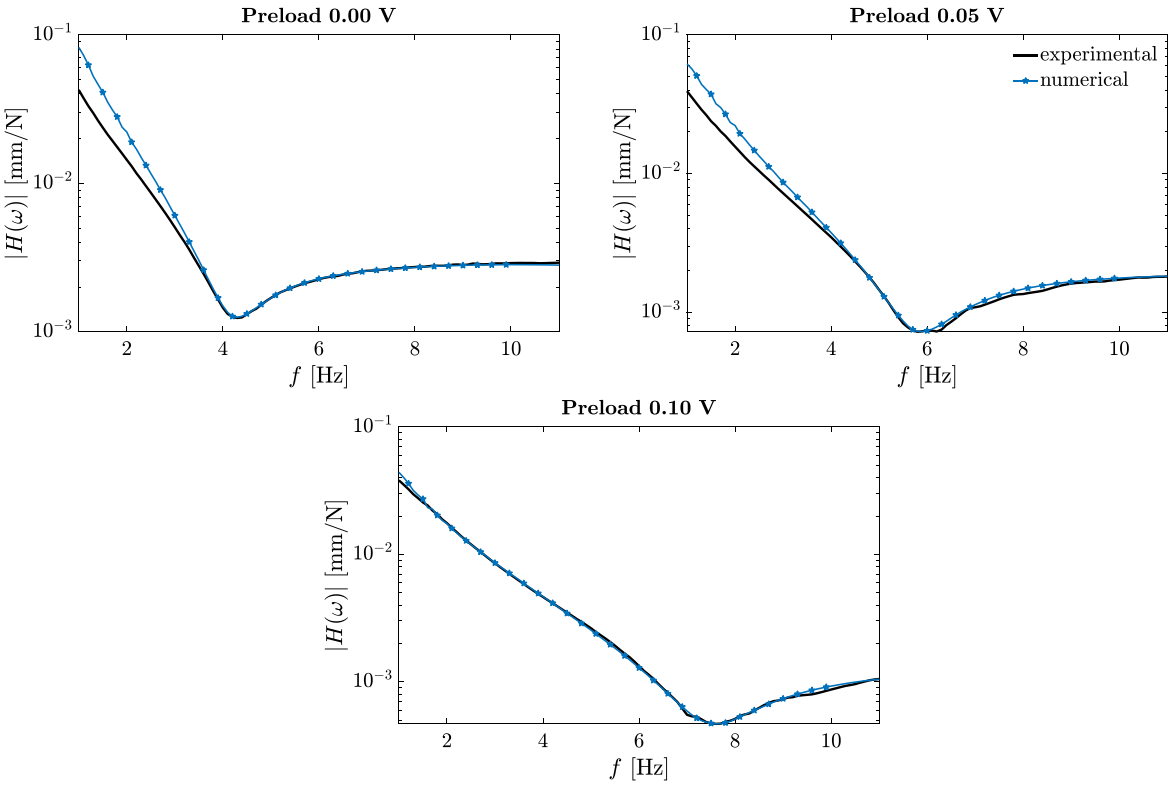

Fig. 17. Experimental (solid black line) versus numerical (solid blue line with markers) receptance response.

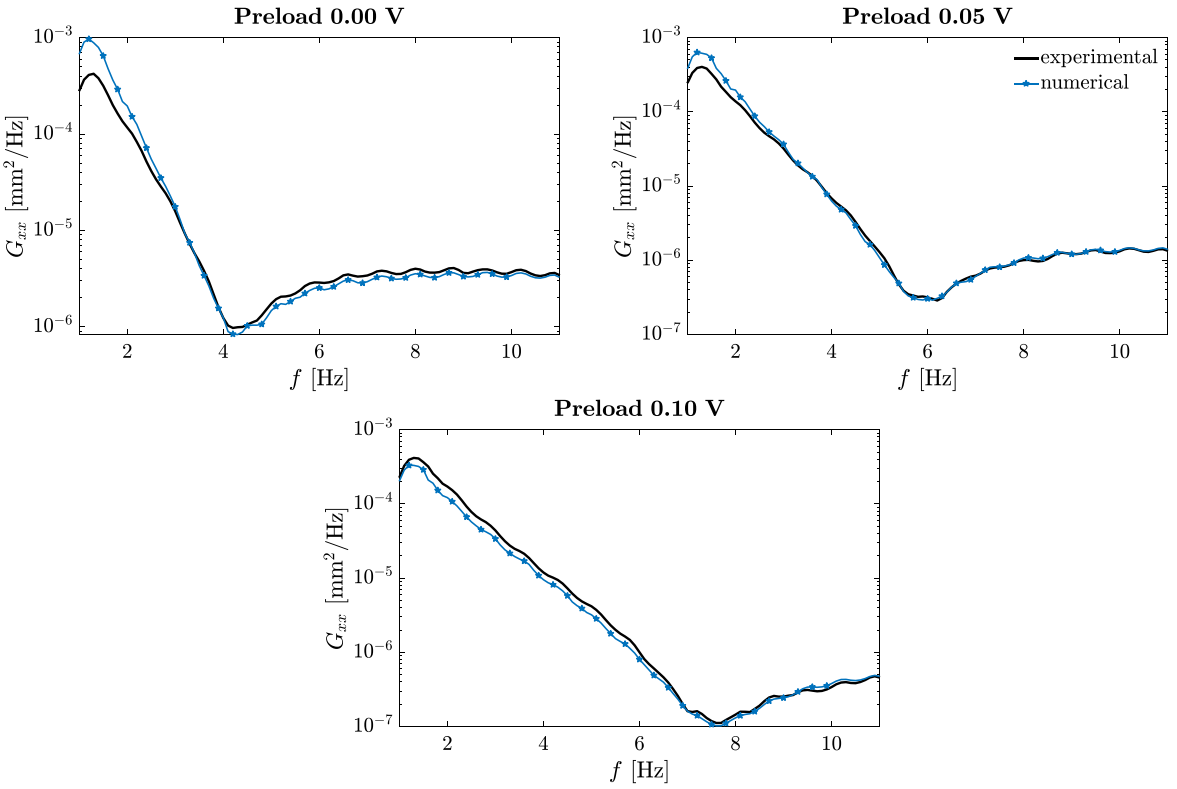

Fig. 18. Experimental (solid black line) versus numerical (solid blue line with markers) PSD response.

and 0.05 V preload are observed. These deviations are also apparent in the time domain, Fig. 19, where the displacements over a period of 10 s are shown. Apart from this, both amplitude and phase of the responses match very well.

As mentioned in Section 3, increasing the amplitude of the input voltage signal for the complete configuration does not result in a significant change in the receptance for a given preload level. For a prestress of 0.05 V and input voltage ranges 0.40–0.60 V and 0.50–0.70 V, respectively, this is shown in Fig. 20 by the solid black and dashed red lines. This behavior is accurately reproduced by the derived mechanical model, as shown by the corresponding lines with markers in Fig. 20. Note that although the receptances are practically unaffected by the change in input voltage amplitudes, the displacement amplitudes in terms of the PSD increase clearly as the input voltage level increases. This comparison shows that the distinct amplitude dependence that occurs in the dry configuration due to the non-linearity related to the dissipation force (Fig. 7) is not so pronounced when the device is filled with water. Moreover, the equally remarkable agreement at a different amplitude range can be considered as an additional evidence of the goodness of the model of the system and identified parameters.

6. Conclusions

In this paper, an innovative passive vibration control device composed of a fluid inerter was studied experimentally. The realized fluid inerter consists of a piston-cylinder equipped with an external tube where a working fluid is conveyed. Based on the experimental outcomes, mechanical models of this control device were developed whose parameters were obtained by numerical optimization. The system was investigated in a frequency range between 0.5 and 12 Hz, performing sine-sweep excitations with various input excitation levels and preload levels. In a first step, the system without working liquid was considered, revealing the nonlinearity due to friction of the piston. A friction model based on the Stribeck effect was successfully employed to capture the dissipation force caused by friction, while simplified models such as Coulomb friction without velocity-dependence of the friction force failed to reproduce the experimental data. Secondly, the complete system with working fluid was investigated and a nonlinearity due to different preload levels was discovered. This was modeled by nonlinear springs representing the compressibility of the fluid and the air trapped in the system. The derived mechanical models were able to reproduce the experimental results in both frequency and time domain.

The following aspects are relevant to a practical implementation of the fluid inerter:

- Although the nonlinearity with respect to the input excitation amplitude appears to be small compared to the system without water, any nonlinearity complicates the design process.

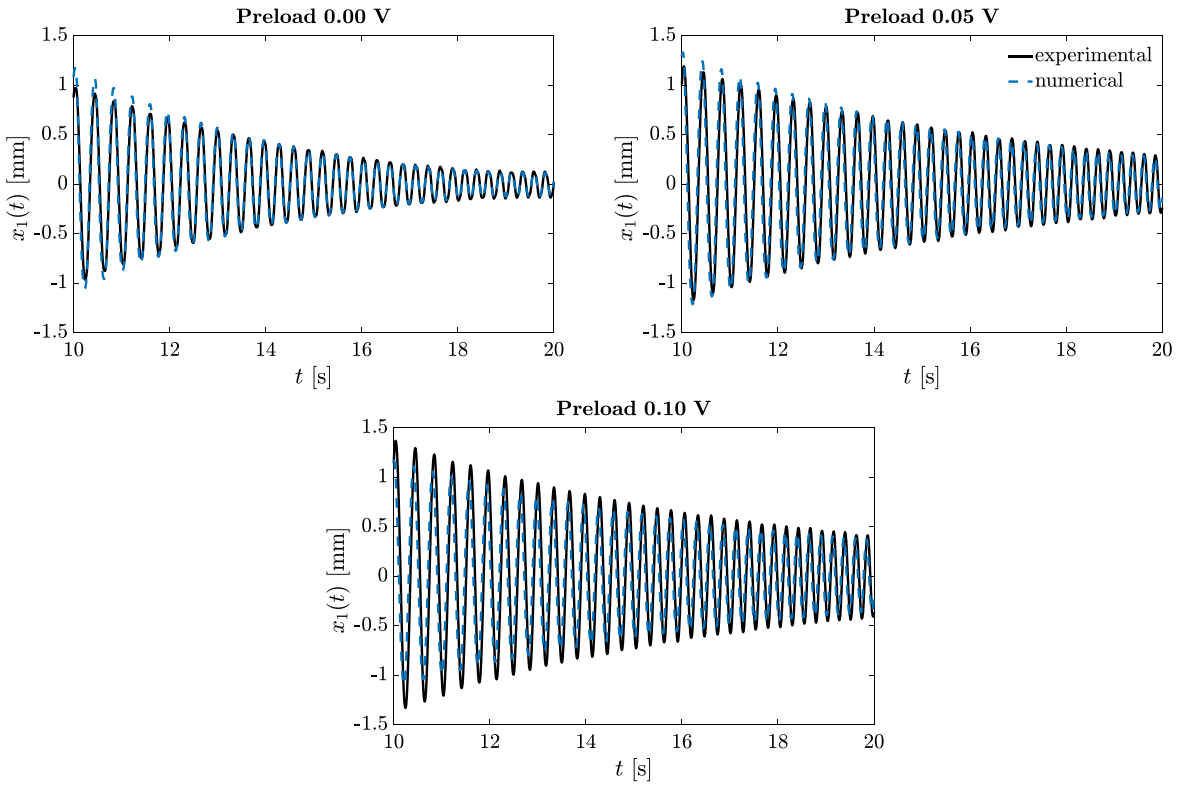

Fig. 19. Experimental (solid black line) versus numerical (dashed blue line) displacement response.

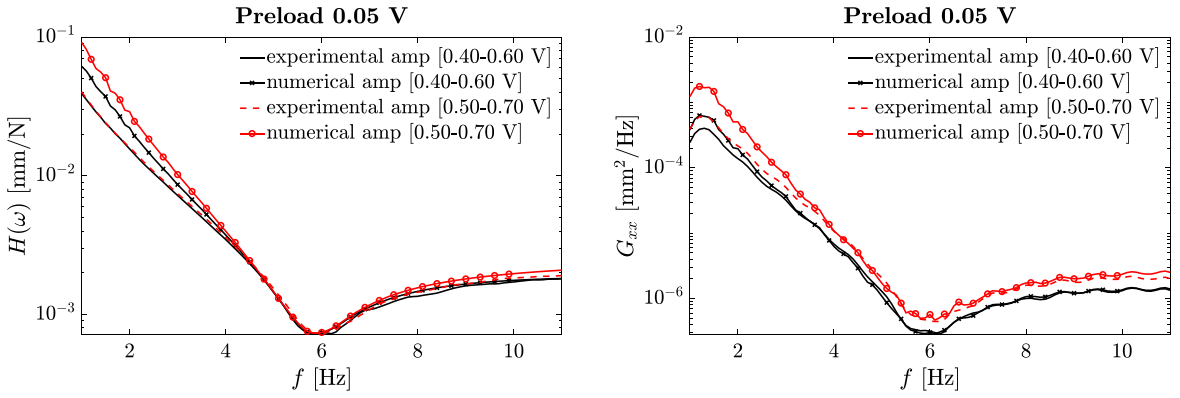

Fig. 20. Experimental versus numerical outcomes in terms of receptance (left) and PSD (right) for two different excitation signal levels and a preload of 0.05 V.

- The anti-resonance observed in the complete configuration limits the practical applicability of the inerter to a frequency range below the anti-resonance frequency. In this respect, preloading the system seems to have a beneficial effect by extending the working frequency range.
- The formation of air bubbles was observed in the experiments, most likely due to cavitation effects.
- Although the influence of this trapped air was successfully modeled and identified as insignificant compared to the preload effect, questions arise in this regard about the long-term stability of the fluid inerter.
- It was possible to generate a fictitious mass (inertance) of about 160 kg with only 50 g of flowing fluid. This underlines the large potential of fluid inerters when applied to vibration control in civil structures.

Future developments might involve the exploitation of the fluid inerter in a large-scale experimental model finalized to analyze possible scaling effects. It is reasonable to assume that nonlinearities as well as cavitation issues and formation of air bubbles

may still occur, however not necessarily proportional to the size of the test rig setup. Moreover, in further studies, the nonlinear mechanical model of a fluid inerter developed in this work will be implemented in the models of passive control devices (Tuned Inerter Dampers, Tuned Mass Damper Inerter, etc.) for more realistic numerical studies. Simulations that are close to reality can indeed minimize the need for experimental tests, which, as seen above, are very costly and time consuming.

CRediT authorship contribution statement

Miriam Chillemi: Conception and design of study, Acquisition of data, Analysis and/or interpretation of data, Writing – original draft. **Thomas Furtmüller:** Conception and design of study, Acquisition of data, Analysis and/or interpretation of data, Writing – original draft, Writing – review & editing. **Christoph Adam:** Conception and design of study, Writing – original draft, Writing – review & editing. **Antonina Pirrotta:** Writing – review & editing.

Declaration of competing interest

The authors declare that they have no known competing financial interests or personal relationships that could have appeared to influence the work reported in this paper.

Data availability

The data that has been used is confidential.

Acknowledgments

This project has received funding from the European Union's Horizon 2020 research and innovation programme under the Marie Skłodowska-Curie grant agreement No 847476. The views and opinions expressed herein do not necessarily reflect those of the European Commission. All authors approved the version of the manuscript to be published.

References

[1] G. Housner, L.A. Bergman, T.K. Caughey, A.G. Chassiakos, R.O. Claus, S.F. Masri, R.E. Skelton, T. Soong, B. Spencer, J.T. Yao, Structural control: past, present, and future, J. Eng. Mech. 123 (9) (1997) 897–971.
[2] O. Altay, Vibration Mitigation Systems in Structural Engineering, 2021, http://dx.doi.org/10.1201/9781315122243.
[3] P. Cristian, L. Septimiu, C. Florentina, R. Victor-Octavian, Structural control systems implemented in civil engineering, Bull. Polytech. Inst. Jassy Constr. Archit. Section LI (LV) (2005).
[4] M.C. Constantinou, T.T. Soong, G.F. Dargush, Passive energy dissipation systems for structural design and retrofit, 1998.
[5] J.P. Den Hartog, Mechanical Vibrations, Courier Corporation, 1985.
[6] B. Schmelzer, M. Oberguggenberger, C. Adam, Efficiency of tuned mass dampers with uncertain parameters on the performance of structures under stochastic excitation, Proc. Inst. Mech. Eng. O 224 (4) (2010) 297–308, http://dx.doi.org/10.1243/1748006XJRR310.
[7] M. Smith, Synthesis of mechanical networks: the inerter, IEEE Trans. Automat. Control 47 (10) (2002) 1648–1662, http://dx.doi.org/10.1109/TAC.2002.803532.
[8] M.C. Smith, The inerter: A retrospective, Annu. Rev. Control Robot. Auton. Syst. 3 (1) (2020) 361–391, http://dx.doi.org/10.1146/annurev-control-053018-023917.
[9] I. Lazar, S. Neild, D. Wagg, Using an inerter-based device for structural vibration suppression, Earthq. Eng. Struct. Dyn. 43 (8) (2014) 1129–1147, http://dx.doi.org/10.1002/eqe.2390.
[10] D. Pietrosanti, M. De Angelis, M. Basili, Optimal design and performance evaluation of systems with tuned mass damper inerter (TMDI), Earthq. Eng. Struct. Dyn. 46 (8) (2017) 1367–1388, http://dx.doi.org/10.1002/eqe.2861.
[11] A. Di Matteo, C. Masnata, C. Adam, A. Pirrotta, Optimal design of tuned liquid column damper inerter for vibration control, Mech. Syst. Signal Process. 167 (2022) 108553, http://dx.doi.org/10.1016/j.ymssp.2021.108553.
[12] J.-S. Hwang, J. Kim, Y.-M. Kim, Rotational inertia dampers with toggle bracing for vibration control of a building structure, Eng. Struct. 29 (6) (2007) 1201–1208, http://dx.doi.org/10.1016/j.engstruct.2006.08.005.
[13] K. Ikago, K. Saito, N. Inoue, Seismic control of single-degree-of-freedom structure using tuned viscous mass damper, Earthq. Eng. Struct. Dyn. 41 (3) (2012) 453–474, http://dx.doi.org/10.1002/eqe.1138.
[14] D. De Domenico, G. Ricciardi, An enhanced base isolation system equipped with optimal tuned mass damper inerter (TMDI), Earthq. Eng. Struct. Dyn. 47 (5) (2018) 1169–1192, http://dx.doi.org/10.1002/eqe.3011.
[15] A. Di Matteo, C. Masnata, A. Pirrotta, Simplified analytical solution for the optimal design of tuned mass damper inerter for base isolated structures, Mech. Syst. Signal Process. 134 (2019) 106337, http://dx.doi.org/10.1016/j.ymssp.2019.106337.
[16] M.C. Smith, Force-controlling mechanical device, 2002, U.S. Patent 7, 316, 303 B2.
[17] F.-C. Wang, M.-S. Hsu, W.-J. Su, T.-C. Lin, Damping and inertial hydraulic device, 2009, U.S. Patent 2009/0108510 A1.
[18] B.J. Gartner, M.C. Smith, Damping and inertial hydraulic device, 2011, U.S. Patent 13/577, 234.
[19] M.Z. Chen, Y. Hu, Inerter and Its Application in Vibration Control Systems, Springer, 2019.
[20] S.J. Swift, M.C. Smith, A.R. Glover, C. Papageorgiou, B. Gartner, N.E. Houghton, Design and modelling of a fluid inerter, Internat. J. Control 86 (11) (2013) 2035–2051, http://dx.doi.org/10.1080/00207179.2013.842263.
[21] M.Z.Q. Chen, M.C. Smith, Restricted complexity network realizations for passive mechanical control, IEEE Trans. Automat. Control 54 (10) (2009) 2290–2301, http://dx.doi.org/10.1109/TAC.2009.2028953.
[22] E. John, D. Wagg, Design and testing of a frictionless mechanical inerter device using living-hinges, J. Franklin Inst. B 356 (14) (2019) 7650–7668, http://dx.doi.org/10.1016/j.jfranklin.2019.01.036.
[23] L. Yuehao, C. Zhe, H. Niaoqing, Y. Yi, Y. Zhengyang, Study of dynamic breakdown of inerter and the improved design, Mech. Syst. Signal Process. 167 (2022) 108520, http://dx.doi.org/10.1016/j.ymssp.2021.108520.

[24] L. Yuehao, C. Zhe, H. Niaoqing, Y. Yi, X. Zhuo, Modeling, design and experiments of a ball-screw inerter with mechanical diodes, J. Sound Vib. 504 (2021) 116121, http://dx.doi.org/10.1016/j.jsv.2021.116121.
[25] S. Sarkar, B. Fitzgerald, Fluid inerter for optimal vibration control of floating offshore wind turbine towers, Eng. Struct. 266 (2022) 114558, http://dx.doi.org/10.1016/j.engstruct.2022.114558.
[26] A. Gonzalez-Buelga, I.F. Lazar, J.Z. Jiang, S.A. Neild, D.J. Inman, Assessing the effect of nonlinearities on the performance of a tuned inerter damper, Struct. Control Health Monit. 24 (3) (2017) e1879, http://dx.doi.org/10.1002/stc.1879.
[27] X. Liu, J.Z. Jiang, B. Titurus, A. Harrison, Model identification methodology for fluid-based inerters, Mech. Syst. Signal Process. 106 (2018) 479–494, http://dx.doi.org/10.1016/j.ymssp.2018.01.018.
[28] D. De Domenico, G. Ricciardi, R. Zhang, Optimal design and seismic performance of tuned fluid inerter applied to structures with friction pendulum isolators, Soil Dyn. Earthq. Eng. 132 (2020) 106099, http://dx.doi.org/10.1016/j.soildyn.2020.106099.
[29] R. Tuluie, Fluid inerter, 2010, U.S. Patent 13/575, 017.
[30] J.S. S. Jaiswal, A. Mikkola, Efficiency comparison of various friction models of a hydraulic cylinder in the framework of multibody system dynamics, Nonlinear Dynam. 104 (4) (2021) 3497–3515, http://dx.doi.org/10.1007/s11071-021-06526-9.
[31] G.F. Lang, D. Snyder, et al., Understanding the physics of electrodynamic shaker performance, Sound Vibr. 35 (10) (2001) 24–33.
[32] A. Dynamic, Instruction manual aps 400 shaker.
[33] T. Furtmüller, A. Di Matteo, C. Adam, A. Pirrotta, Base-isolated structure equipped with tuned liquid column damper: An experimental study, Mech. Syst. Signal Process. 116 (2019) 816–831, http://dx.doi.org/10.1016/j.ymssp.2018.06.048.
[34] A. Zangwill, Modern Electrodynamics, Cambridge University Press, 2012, http://dx.doi.org/10.1017/CBO9781139034777.
[35] Y. Shen, L. Chen, Y. Liu, X. Zhang, X. Yang, Optimized modeling and experiment test of a fluid inerter, J. Vibroengineering 18 (5) (2016) 2789–2800, http://dx.doi.org/10.21595/jve.2016.16885.
[36] L.C. Bo, D. Pavelescu, The friction-speed relation and its influence on the critical velocity of stick-slip motion, Wear 82 (3) (1982) 277–289, http://dx.doi.org/10.1016/0043-1648(82)90223-X.
[37] P. Brown, J. McPhee, A continuous velocity-based friction model for dynamics and control with physically meaningful parameters, J. Comput. Nonlinear Dyn. 11 (5) (2016) http://dx.doi.org/10.1115/1.4033658.
[38] S. Bhattacharyya, A.D. Ghosh, B. Basu, Nonlinear modeling and validation of air spring effects in a sealed tuned liquid column damper for structural control, J. Sound Vib. 410 (2017) 269–286, http://dx.doi.org/10.1016/j.jsv.2017.07.046.